Why is El Niño warm?

Allison K. Hogikyan[1*], Laure Resplandy[2,3], Stephan Fueglistaler[1,2],

[1]Princeton University, Atmospheric and Oceanic Sciences Program

[2]Princeton University Department of Geosciences

[3]Princeton University High Meadows Environmental Institute

Key Points:

- Tropics-wide warming during El Niño due to warming of the warm ocean regions with deep convection
- The warming of warm regions results from a decrease in evaporation driven by surface winds
- Anomalous atmospheric large-scale circulation leads to wind decrease and explains prominent warming

[*]Current address, 300 Forrestal Road, Sayre Hall, Princeton NJ 08540

Corresponding author: A. K. Hogikyan, hogikyan@princeton.edu

Abstract

The geographic rearrangement of the tropical oceanic and atmospheric circulation during an El Niño event is associated with a well-understood strong surface warming of the climatologically cold eastern equatorial Pacific. However, the concomitant warming of the warmest waters where deep convection occurs - responsible for the tropics-wide free tropospheric warming- is less well understood. Here, we show that in both a coupled atmosphere-ocean climate model and in reanalysis data, El Niño is associated with an increase in evaporation over the colder $\sim 70\%$, but with a decrease in evaporation over the warmest $\sim$ 30% of the tropical oceans where atmospheric deep convection connects the surface with the free troposphere. The reduction in evaporation is driven by a weakening of the near-surface winds. We propose that the prominent tropics-wide warming during El Niño is a consequence of the reduction of near-surface winds in regions of deep convection due to the anomalous large-scale circulation.

Plain Language Summary

El Niño events are associated with a well-understood strong surface warming of the climatologically cold eastern equatorial Pacific and a less-well understood increase in global-mean surface and atmospheric temperatures. The warming of the warmest waters where atmospheric deep convection occurs is responsible for the tropics-wide free tropospheric warming, which is the first step in communicating the warm anomaly beyond the equatorial Pacific. We find that a decrease in surface wind speed, tied to the weakening of the Walker circulation, controls the surface energy budget and warming of these regions.

1 Introduction

The El Niño/Southern Oscillation (ENSO) is the largest source of natural variability in the climate system and strongly modulates global atmospheric and surface temperatures. Warm ENSO events, El Niño events, are characterized by a slowing of the wind-driven upwelling of cold water in the eastern equatorial Pacific. This causes the sea surface temperature (SST) to increase in this otherwise cold tropical region (Bjerknes, 1969; S. G. H. Philander, 1983). This ocean-forced positive SST anomaly increases local evaporation, acting as a negative feedback that moderates the surface warming in this region (Trenberth, 2002; W. Wang & McPhaden, 2000).

El Niño events are identified and their strength quantified by the warming in the east Pacific (Trenberth, 1997), but their impact is global, communicated through a warming of the tropical free troposphere and geographical rearrangement of atmospheric convection (Rasmusson & Wallace, 1983; Lintner & Chiang, 2005; Seager et al., 2003; Chiang & Sobel, 2002; Klein et al., 1999; Yulaeva & Wallace, 1994; Alexander et al., 2002; Lau & Nath, 1996). The rearrangement of convection (Figure 1a, b) weakens the Walker circulation (e.g. S. G. H. Philander (1983)), strengthens the zonal-mean Hadley circulation (Lu et al., 2008; Seager et al., 2003), and induces a planetary wave that affects extratropical weather patterns (Rasmusson & Wallace, 1983). Both the weakening of the Walker cell and the warming of the free troposphere can affect SSTs in the tropical Atlantic and Indian Oceans (Chiang & Sobel, 2002; Lohmann & Latif, 2007). This tropics-wide, and eventually global, warming during El Niño events primarily results from the warming of the warmest regions of the tropical oceans where atmospheric deep convection connects the surface and the free troposphere (e.g. Sobel et al. (2002); Brown and Bretherton (1997)). Thus, in order to understand the prominent tropics-wide warming signal during El Niño, one must ask what processes allow the SSTs in the warmest regions to increase.

It is recognized that the surface energy budget of the warmest regions, where the thermocline is deep, can be strongly affected by changes in evaporation driven by surface wind anomalies associated with the response of the Walker circulation to ENSO. Specifically, part of the eastward shift of the local SST maximum during El Niño has been attributed to the change in the zonal structure of the zonal wind over the warm pool (B. Wang, 1995). Here, we argue that the change in the zonal wind not only leads to the eastward displacement of the local SST maximum, but is also responsible for the tropical average warming during El Niño relative to the climatological base state.

We use a pre-industrial control experiment in a coupled atmosphere-ocean global climate model (GCM) and the fifth-generation ECMWF Reanalysis (ERA5), a reconstruction of the climate state over the period 1979-2019. In the colder parts of the tropical oceans, evaporation increases when the surface warms. This negative feedback is the expected response of the surface energy budget to the reduced upwelling of cold waters (Trenberth, 2002; W. Wang & McPhaden, 2000; Lloyd et al., 2011). Conversely, we find that evaporation decreases in the warm regions where atmospheric deep convection occurs. This decrease in evaporation is associated with a decrease in surface wind speed.

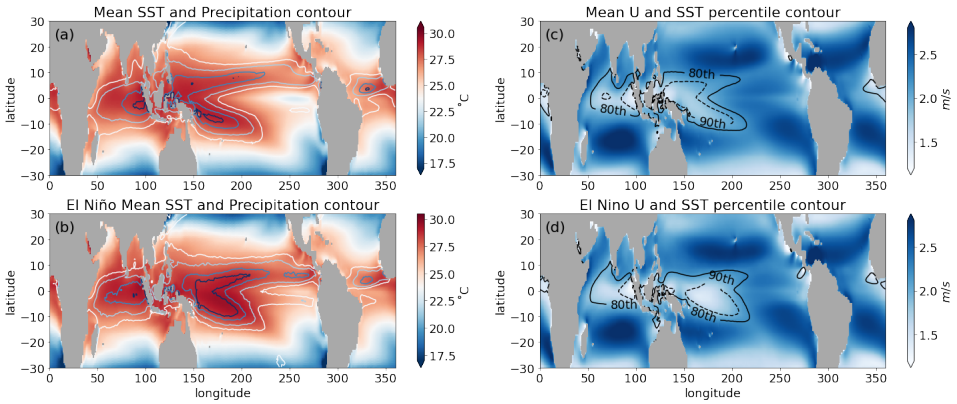

Figure 1. Mean and El Niño SST and surface winds in GFDL-FLOR (a, b) SST with contours of precipitation intensity simulated by GFDL-FLOR preindustrial control experiment. Darker blue contours represent more intense precipitation. (c, d) The simulated near-surface wind speed with contours of 80^{th} (solid) and 90^{th} (dashed) percentiles of SST. The wind speed shown only includes winds resolved on the model grid (U=$\sqrt{u^2+v^2}$). The lower row (panels b, d) only includes months in the experiment when the normalized Niño3.4 index exceeds 0.6.

We therefore propose that the anomalous large-scale circulation leads to the prominent tropics-wide warming by decreasing near-surface wind speeds over the sea surface where convection occurs. The resulting decrease in evaporation leads to the surface warming, which atmospheric convection then communicates to the free troposphere.

2 Data and Methods

2.1 GFDL-FLOR coupled model

We analyze the behavior of ENSO in the Forecast Oriented Low Ocean Resolution configuration of the Geophysical Fluid Dynamics Laboratory (GFDL) coupled climate model, referred to as FLOR (Vecchi et al., 2014). This model uses the nominal 1° resolution ocean and sea ice model from GFDL-CM2.1 (Delworth et al., 2006) but a higher resolution (0.5°) atmosphere from the GFDL-CM2.5 (Delworth et al., 2012) model and an improved land model (LM3, (Milly et al., 2014)). The ocean resolution telescopes to 0.333° meridional spacing near the equator. We use 100 years of FLOR results from a pre-industrial control experiment, in which atmospheric CO_2 concentrations, aerosol and solar forcing are prescribed at 1860 levels (Yang et al., 2019).

2.2 ECMWF Reanalysis

We also use data from the European Centre for Medium-Range Weather Forecasts (ECMWF) reanalysis (ERA5), a reconstruction of the climate state since 1979. ERA5 assimilates historical observations onto a global 30km grid (Hersbach et al., 2019). Long-term linear trends are removed at each location. We analyze the time period January 1979 to February 2019, which includes seven El Niño events (1982-83, 1986-87, 1991-92, 1997-98, 2002-03, 2009-10, 2014-15).

2.3 SST Percentiles

In order to differentiate the behavior at warm and cold SSTs without imposing a temperature or precipitation threshold, we organize surface (2D) fields by SST. After sorting the tropical (30°S:30°N) SSTs from coldest (0th percentile) to warmest (100th percentile), we average each variable into one hundred equal-area bins, which we refer to as SST percentiles.

2.4 Oceanic Mixed Layer Heat Budget

A simple mixed layer budget reveals the importance of surface heat fluxes for the warm anomaly at the highest SSTs. A change in mixed layer temperature T_{ML} over a time interval (in this case, the anomalous surface warming during El Niño) results from either the surface heat flux ($\mathcal{Q}_{\mathrm{sfc}}$) or oceanic advection and mixing, as denoted below.

$$\int_{t_1}^{t_2} dT_{\mathrm{ML},Q_{\mathrm{sfc}}} + dT_{\mathrm{ML,Oc}} = \Delta T_{\mathrm{ML},Q_{\mathrm{sfc}}} + \Delta T_{\mathrm{ML,Oc}} = \Delta T_{\mathrm{ML}} \approx \Delta SST \tag{1}$$

where $dT_{\mathrm{ML},Q_{\mathrm{sfc}}} = \frac{\mathcal{Q}_{\mathrm{sfc}}}{\rho c_p H_{\mathrm{ML}}} \partial t$, $\mathcal{Q}_{\mathrm{sfc}}$ is defined as the net radiative, latent and sensible fluxes at the air-sea interface ($\mathcal{Q}_{\mathrm{sfc}} = \mathcal{R}_{\mathrm{dn}} - \mathcal{R}_{\mathrm{up}} - \mathcal{L} - \mathcal{S}$), t is time, ρ is the density of seawater, c_p is the heat capacity of seawater, and H_{ML} is the depth of the mixed layer, defined as the depth where the density is $0.03 \frac{\mathrm{kg}}{\mathrm{m}^3}$ greater than at the surface. We estimate the temperature change due to ocean processes $dT_{\mathrm{ML,Oc}}$ as a residual from Equation 1. Note that T_{ML} approximates the SST very closely.

To account for the anomalous SST increase during El Niño events, we remove the monthly-mean seasonal cycle and then integrate the anomalous ocean and surface forcings during the growth phase of each event. The growth phase is defined to be between the month of July, when the Niño 3.4 index first becomes positive, and the month of Jan-

uary, after the peak of the index (Figure 2). The integrated forcings during this time period approximately account for the SST increase from the beginning of July to the beginning of February.

2.5 Controls on Latent Heat Flux

The latent heat flux $\mathcal{L}$ is proportional to the surface moisture deficit Δq, the surface wind speed W, and properties of the air-sea interface according to the bulk formula for evaporation:

$$\mathcal{L} = \mathrm{L} \cdot C_\mathrm{E} \cdot \rho_\mathrm{a} \cdot \mathrm{W} \cdot \Delta q \tag{2}$$

L is the specific latent heat of evaporation, C_E is the bulk transfer coefficient for evaporation, ρ_a is the density of the near-surface air, $\Delta q = q^*_\mathrm{sfc} - q_\mathrm{2m}$, the difference between the saturation specific humidity at SST and the near surface (2 meter) humidity, and W is the wind speed at the surface (Large & Yeager, 2009). We find that variations in $\mathcal{L}$ are dominated by changes in W and Δq, and write:

$$\frac{\mathcal{L}'}{\langle \mathcal{L} \rangle} = \frac{W'}{\langle W \rangle} + \frac{\Delta q'}{\langle \Delta q \rangle} + R \tag{3}$$

where R is the residual and all terms are monthly means. Primes (X') represent anomalies from the seasonal cycle while brackets ($\langle X \rangle$) are the climatological monthly mean values of the variable X. We take the latent heat flux to be positive when it is from the ocean to the atmosphere. R includes variations in C_E and ρ_a as well as covariation on sub-monthly time scales of the wind speed and humidity deficit. It is small relative to the other terms (Figure 3a) and we do not discuss it further.

We use slightly different methods to calculate Δq from the ERA5 and GFDL-FLOR data. In both cases, q^*_sfc is calculated from the SST. We use the two meter relative humidity and q^*_sfc to calculate q_2m from GFDL-FLOR, whereas in ERA5, q_2m is calculated from the two meter dewpoint temperature. We utilize additional information about the calculation of W in GFDL-FLOR in Section 3.2.

3 Results

3.1 Air-sea heat flux warms the warmest SSTs

Figure 2 shows the average evolution of the SST anomaly during an El Niño event. Tropical SSTs are sorted from coldest to warmest in what we call SST percentiles (See

Methods). While certain regions may warm (e.g. east Pacific) or cool (e.g. west Pacific), sorting into SST bins makes it clear that all percentiles warm (see also Sobel et al. (2002); Fueglistaler (2019)).

In order to identify which are the 'warmest SSTs' relevant for variations in free tropospheric temperature, we identify where convection is concentrated in SST percentiles. With precipitation as a proxy, it is clear that convection is largely confined to the warmest 30% of the tropics (Figure 3a). This is also the area with SSTs equal or higher than about 27°C, the well-known approximate threshold for deep convection in the current climate (Graham & Barnett, 1987).

In both GFDL-FLOR and ERA5, the surface warming of cold percentiles (0-60 percentiles) is attributed to oceanic forcing (advection and mixing), while surface heat fluxes have a cooling effect that partially offsets the oceanic influence (Figure 2a,c). The SST anomaly in low and middle percentiles begins to emerge in boreal fall prior to the peak of the event (Figure 2b,d). As the surface warms, the evaporation rate increases so that $\mathcal{Q}_{\text{sfc}}$ opposes the surface warming (W. Wang & McPhaden, 2000; Lloyd et al., 2011). This is consistent with the expectation that the signal seen in colder percentile bins should be associated with the decrease in the Pacific upwelling and vertical mixing. The SST anomaly in the cold percentiles in Figure 2(a, c) is small compared to the warming of the upwelling region in the equatorial Eastern Pacific. This is largely due to the fact that this region is relatively small and other regions may not or only weakly warm due to other processes (Chiang & Sobel, 2002; Lintner & Chiang, 2005; Klein et al., 1999). Thus, the strong warming in this region primarily leads to a shuffling in rank in percentile space. The peak warming at the warmest SSTs (70-100 percentiles) is in February-March, after that of the colder SSTs (Figure 2b,d). Since the Niño3.4 index is based on SST anomalies at the cold SSTs, the El Niño warm anomaly in warm percentiles peaks later than the Niño3.4 index. Consistent with our expectation that the warmest SSTs determine the temperature of the tropical troposphere, the peak in the warm anomaly in the tropical troposphere is also delayed from that of the Niño3.4 index (Sobel et al., 2002; Fueglistaler, 2019).

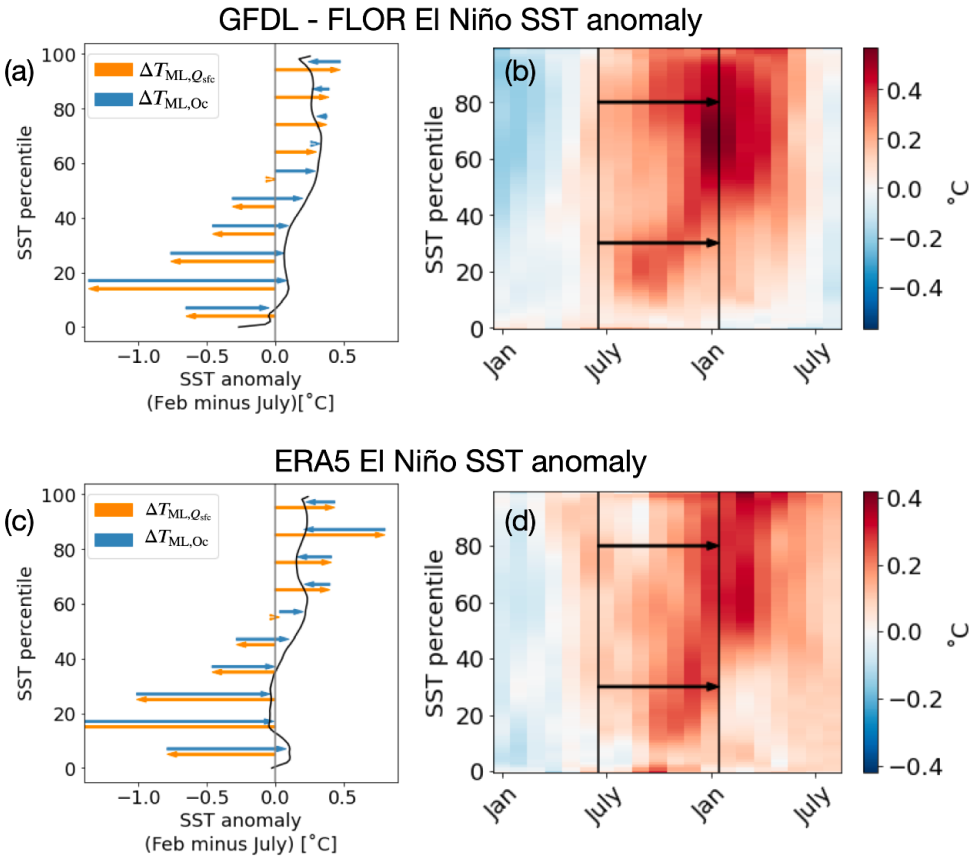

Figure 2. Contributions to ocean mixed-layer temperature increase during El Niño. (a, c) ΔT_{ML} ($\approx$ ΔSST) at each percentile bin in the global tropics (30S:30N). $\Delta T_{\mathrm{ML},Q_{\mathrm{sfc}}}$ is represented by orange arrows and $\Delta T_{\mathrm{ML,Oc}}$ by blue arrows (calculated as a residual), both averaged over deciles (0-9th percentile, 10-19th percentile, etc.). (b, d) T_{ML} anomaly during an El Niño event, composited on the calendar year. Black lines are the limits for the integral represented in (a, c).

3.2 Latent heat flux anomaly at the warmest SSTs a function of wind speed

At both cold and warm SSTs, the latent heat flux is the largest component of the surface heat flux anomaly (not shown). In order to attribute the latent heat flux ($\mathcal{L}$) anomaly to a surface forcing, in Figure 3 we show the mean El Niño $\mathcal{L}$ anomaly in SST percentiles, and then separate it into contributions from humidity and wind speed following Equation 3.

Consistent with prior studies (W. Wang & McPhaden, 2000; Lloyd et al., 2011), we find that the changes in the surface energy budget in the colder 70 percentiles are such that the changes in the latent heat flux are following, not forcing, the surface temperature change. The saturation specific humidity increases when the surface warms but the near-surface humidity does not keep up and as a result, the humidity deficit (Δq) increases. Changes in the wind speed are overwhelmed by the increase in the humidity deficit, so evaporation increases. This is in line with the intuitive expectation of an increase in evaporation with warming (Eqn. 3, Figure 3b,e).

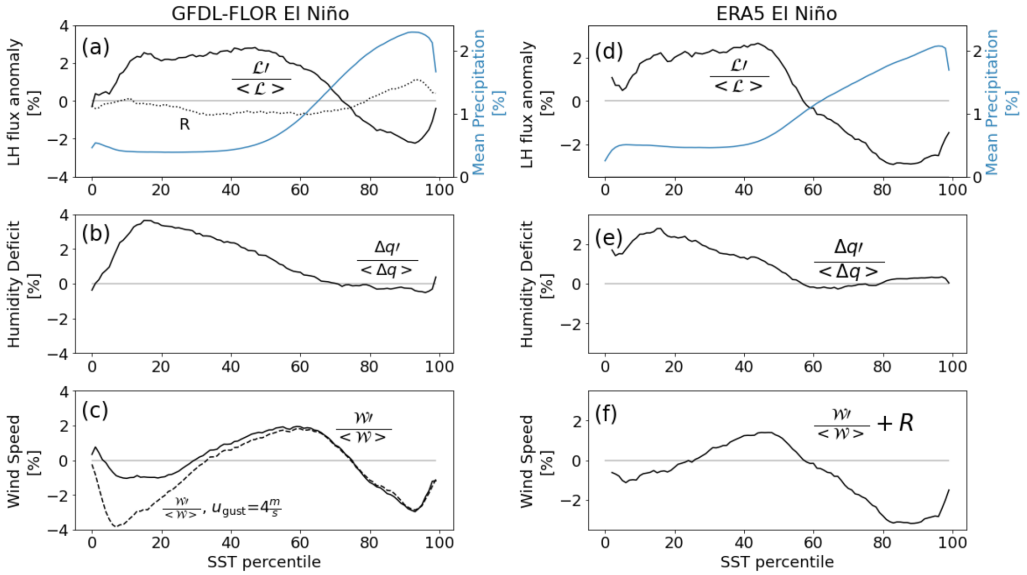

Figure 3. Contributions to latent heat flux anomaly during El Niño Top (a, d): Latent heat flux ($\mathcal{L}$) anomaly and mean distribution of precipitation. Middle (b, e): humidity deficit (Δq) anomaly. Bottom (c, f): anomaly in the surface wind speed W. Solid lines in (b, c) approximate the solid black line in (a) with the residual R shown as the dotted line in panel (a) (Equation 3). (c) also shows an estimate of the wind speed anomaly (W) if the gustiness (u_{gust}) is held constant at 4ms^{-1}. The wind speed anomaly shown in (f) is estimated as the residual of (d, e). All variables are sorted from coldest to warmest SST.

Counter to this intuition, $\mathcal{L}$ decreases in the warmest 30 percentiles during El Niño despite a surface warming (Figure 3a, d, Figure 2). The decrease in $\mathcal{L}$ accounts for much of the decrease in surface heat flux found in Section 3.1.

Figure 3(b, c) shows that the humidity deficit at warm SSTs does not change in response to El Niño but a decrease in wind speed leads to the decrease in evaporation in GFDL-FLOR. The total wind speed W used for flux calculations in GFDL-FLOR includes parameterized sub-grid scale winds we refer to as 'gustiness,' u_{gust} (Beljaars, 1995) as well as the winds (u, v) resolved on the model grid ($\text{W} = \sqrt{u^2 + v^2 + u_{\text{gust}}^2}$). We find there is very little change in the gustiness during El Niño and the resolved winds drive the decrease in wind speed. As a result, the anomaly in the total wind speed W is well approximated by replacing u_{gust} with a constant near its mean value (Figure 3c). The zonal winds are responsible for the decreased wind speed (not shown), suggesting the weakened Walker circulation may play a role in forcing the warming of the warmest SSTs.

Similarly, in ERA5, there is no anomaly in humidity deficit and instead a reduction in wind speed drives the decreased $\mathcal{L}$ at warm SSTs (Figure 3d, e, f). The ERA5 dataset also suggests that the zonal winds are the source of the strong negative wind speed anomaly in warm percentiles, as found in GFDL-FLOR (not shown).

3.3 Positive feedback from longwave radiation

The longwave radiative flux (not shown) is also an important contributor to the anomalous surface heat flux at the warmest SSTs, but is a feature of and not a forcing for the warming. When the surface and boundary layer warm, the increased downward longwave flux from the atmosphere is greater than the increased upward longwave flux from the surface. The increased downward longwave flux from the atmosphere is due not only to the warming of the atmosphere but also the increased humidity (Allan, 2006). The longwave flux anomaly can be explained as a (local) positive feedback, whereas no such argument applies to the wind speed. Thus, the change in wind appears to be the forcing responsible for the warming at the warmest SSTs.

3.4 La Niña parallels El Niño

We find that during the cold phase of ENSO, termed La Niña (S. G. Philander, 1990), the same mechanism leads to a cooling in the oceanic regions with deep atmospheric convection. The cold anomaly at cold SSTs is associated with ocean processes, consistent with the expectation that the intensification of the wind-driven upwelling provides a strong signal in lower percentiles. On the other hand, surface heat fluxes are responsible for the

cold anomaly in the warmest 30 percentiles (Appendix, Figure A1). An increase in surface wind speed, primarily due to meridional winds (not shown), leads to an increase in evaporation which cools the warmest SSTs (Appendix, Figure A2).

4 Conclusions

The warming of the tropical free troposphere during El Niño is due to a warming of the surface in regions with atmospheric deep convection. We find the warm SST anomaly there is not due to local ocean dynamics, but results from a surface heat flux anomaly. The surface heat flux anomaly can be traced back to a decrease in the surface wind speed (primarily the zonal component) which damps evaporation. Since the surface wind speed in the regions with atmospheric deep convection is lower during El Niño than in the climatic base state, the highest SSTs in the El Niño state are higher than in the base state, leading to the prominent atmospheric warming.

The results presented here may also have ramifications for theory and idealized modeling of ocean-atmosphere coupling. We have shown that the latent heat flux over tropical oceans does not vary as a function of SST alone, although it has been parameterized as such in simple models of tropical Pacific SST variability, including models of the response to anthropogenic forcing (Seager et al., 1988, 2019; Vialard et al., 2001).

The wind-forced ocean heat uptake anomaly in the warm regions partially opposes the heat flux anomaly in the upwelling regions, where oceanic heat uptake is reduced (W. Wang & McPhaden, 2000; Trenberth et al., 2002; Lloyd et al., 2011). This interplay between heat uptake in colder and warmer parts of the tropics may also affect longer-term variations in ocean heat uptake and temperature trends(Watanabe et al., 2020; Po-Chedley et al., 2021). Future work will investigate its role in decadal modes such as the Interdecadal Pacific Oscillation, the primary mode of decadal climate variability in the Pacific Ocean, which may contribute to variations in the global mean surface temperature that are caused by changes to the rate of ocean heat uptake (Xie et al., 2016).

Acknowledgments

A.K.H. acknowledges support from the National Science Foundation Graduate Research Fellowship Program under Grant No. DGE-2039656. Any opinions, findings, and conclusions or recommendations expressed in this material are those of the author and

do not necessarily reflect the views of the National Science Foundation. The authors thank Wenchang Yang for making available the FLOR pre-industrial control experiment (Yang et al., 2019). ERA5 data was downloaded from the Copernicus Climate Data Store in January 2020 (Hersbach et al., 2019). The FLOR result used in this study is hosted by Dataspace (https://doi.org/10.34770/g7fe-hs07). The authors declare no competing financial interests.

References

Alexander, M. A., Bladé, I., Newman, M., Lanzante, J. R., Lau, N.-C., & Scott, J. D. (2002). The atmospheric bridge: The influence of enso teleconnections on air–sea interaction over the global oceans. *Journal of climate*, *15*(16), 2205–2231.

Allan, R. P. (2006). Variability in clear-sky longwave radiative cooling of the atmosphere. *Journal of Geophysical Research*, *111*. doi: 10.1029/2006JD007304

Beljaars, A. C. (1995). The parametrization of surface fluxes in large-scale models under free convection. *Quarterly Journal of the Royal Meteorological Society*, *121*(522), 255–270.

Bjerknes, J. (1969). Atmospheric teleconnections from the equatorial pacific. *Monthly weather review*, *97*(3), 163–172.

Brown, R. G., & Bretherton, C. S. (1997). A test of the strict quasi-equilibrium theory on long time and space scales. *Journal of the Atmospheric Sciences*, *54*(5), 624–638. doi: 10.1175/1520-0469(1997)054⟨0624:ATOTSQ⟩2.0.CO;2

Chiang, J. C. H., & Sobel, A. H. (2002). Tropical tropospheric temperature variations caused by ENSO and their influence on the remote tropical climate*. *Journal of Climate*, *15*(18), 2616–2631. doi: 10.1175/1520-0442(2002)015⟨2616:TTTVCB⟩2.0.CO;2

Delworth, T. L., Broccoli, A. J., Rosati, A., Stouffer, R. J., Balaji, V., Beesley, J. A., ... Zhang, R. (2006). GFDL's CM2 global coupled climate models. part i: Formulation and simulation characteristics. *Journal of Climate*, *19*(5), 643–674. doi: 10.1175/JCLI3629.1

Delworth, T. L., Rosati, A., Anderson, W., Adcroft, A. J., Balaji, V., Benson, R., ... Zhang, R. (2012). Simulated climate and climate change in the GFDL CM2.5 high-resolution coupled climate model. *Journal of Climate*, *25*(8), 2755–2781.

doi: 10.1175/JCLI-D-11-00316.1

Fueglistaler, S. (2019). Observational evidence for two modes of coupling between sea surface temperatures, tropospheric temperature profile, and shortwave cloud radiative effect in the tropics. *Geophysical Research Letters*, *46*(16), 9890–9898. doi: 10.1029/2019GL083990

Graham, N. E., & Barnett, T. P. (1987). Sea surface temperature, surface wind divergence, and convection over tropical oceans. *Science*, *238*(4827), 657–659.

Hersbach, H., Bell, B., Berrisford, P., Biavati, G., Horányi, A., Muñoz Sabater, J., ... others (2019). Era5 monthly averaged data on single levels from 1979 to present. *Copernicus Climate Change Service (C3S) Climate Data Store (CDS)*, *10*.

Klein, S. A., Soden, B. J., & Lau, N.-C. (1999). Remote sea surface temperature variations during ENSO: Evidence for a tropical atmospheric bridge. *Journal of Climate*, *12*(4), 917–932. doi: 10.1175/1520-0442(1999)012⟨0917:RSSTVD⟩2.0.CO;2

Large, W. G., & Yeager, S. G. (2009). The global climatology of an interannually varying air–sea flux data set. *Climate Dynamics*, *33*(2), 341–364. doi: 10.1007/s00382-008-0441-3

Lau, N.-C., & Nath, M. J. (1996). The role of the "atmospheric bridge" in linking tropical pacific enso events to extratropical sst anomalies. *Journal of Climate*, *9*(9), 2036–2057.

Lintner, B. R., & Chiang, J. C. H. (2005). Reorganization of tropical climate during el niño: A weak temperature gradient approach. *Journal of Climate*, *18*(24), 5312–5329. doi: 10.1175/JCLI3580.1

Lloyd, J., Guilyardi, E., & Weller, H. (2011). The role of atmosphere feedbacks during ENSO in the CMIP3 models. part II: using AMIP runs to understand the heat flux feedback mechanisms. *Climate Dynamics*, *37*(7), 1271–1292. doi: 10.1007/s00382-010-0895-y

Lohmann, K., & Latif, M. (2007). Influence of el niño on the upper-ocean circulation in the tropical atlantic ocean. *Journal of Climate*, *20*(19), 5012–5018. doi: 10.1175/JCLI4292.1

Lu, J., Chen, G., & Frierson, D. M. W. (2008). Response of the zonal mean atmospheric circulation to el niño versus global warming. *Journal of Climate*,

21(22), 5835–5851. doi: 10.1175/2008JCLI2200.1

Milly, P. C., Malyshev, S. L., Shevliakova, E., Dunne, K. A., Findell, K. L., Gleeson, T., ... Swenson, S. (2014). An enhanced model of land water and energy for global hydrologic and earth-system studies. *Journal of Hydrometeorology*, *15*(5), 1739–1761.

Philander, S. G. (1990). El niño, la niña, and the southern oscillation. *International Geophysics Series*, *46*, 9–11.

Philander, S. G. H. (1983). El niño southern oscillation phenomena. *Nature*, *302*(5906), 295–301. doi: 10.1038/302295a0

Po-Chedley, S., Santer, B. D., Fueglistaler, S., Zelinka, M. D., Cameron-Smith, P. J., Painter, J. F., & Fu, Q. (2021). Natural variability contributes to model–satellite differences in tropical tropospheric warming. *Proc. Nat. Acad. of Sciences*, *118*(13), e2020962118. doi: 10.1073/pnas.2020962118

Rasmusson, E. M., & Wallace, J. M. (1983). Meterological aspects of the el niño/southern oscillation. *Science*, *222*(4629), 1195–1202.

Seager, R., Cane, M., Henderson, N., Lee, D.-E., Abernathey, R., & Zhang, H. (2019). Strengthening tropical pacific zonal sea surface temperature gradient consistent with rising greenhouse gases. *Nature Climate Change*, *9*(7), 517–522. doi: 10.1038/s41558-019-0505-x

Seager, R., Harnik, N., Kushnir, Y., Robinson, W., & Miller, J. (2003). Mechanisms of hemispherically symmetric climate variability. *Journal of Climate*, *16*(18), 2960–2978. doi: 10.1175/1520-0442(2003)016⟨2960:MOHSCV⟩2.0.CO;2

Seager, R., Zebiak, S. E., & Cane, M. A. (1988). A model of the tropical pacific sea surface temperature climatology. *Journal of Geophysical Research: Oceans*, *93*, 1265–1280. doi: https://doi.org/10.1029/JC093iC02p01265

Sobel, A. H., Held, I. M., & Bretherton, C. S. (2002). The ENSO signal in tropical tropospheric temperature. *Journal of Climate*, *15*(18), 2702–2706. doi: 10.1175/1520-0442(2002)015⟨2702:TESITT⟩2.0.CO;2

Trenberth, K. E. (1997). The definition of el niño. *Bulletin of the American Meteorological Society*, *78*(12), 2771–2777. doi: 10.1175/1520-0477(1997)078⟨2771:TDOENO⟩2.0.CO;2

Trenberth, K. E. (2002). Evolution of el niño–southern oscillation and global atmospheric surface temperatures. *Journal of Geophysical Research*, *107*. doi: 10

.1029/2000JD000298

Trenberth, K. E., Stepaniak, D. P., & Caron, J. M. (2002). Interannual variations in the atmospheric heat budget. *Journal of Geophysical Research*, *107*. doi: 10.1029/2000JD000297

Vecchi, G. A., Delworth, T., Gudgel, R., Kapnick, S., Rosati, A., Wittenberg, A. T., ... Zhang, S. (2014). On the seasonal forecasting of regional tropical cyclone activity. *Journal of Climate*, *27*(21), 7994–8016. doi: 10.1175/JCLI-D-14-00158.1

Vialard, J., Menkes, C., Boulanger, J.-P., Delecluse, P., Guilyardi, E., McPhaden, M. J., & Madec, G. (2001). A model study of oceanic mechanisms affecting equatorial pacific sea surface temperature during the 1997–98 el niño. *Journal of Physical Oceanography*, *31*(7), 1649–1675. doi: 10.1175/1520-0485(2001)031⟨1649:AMSOOM⟩2.0.CO;2

Wang, B. (1995). Transition from a cold to a warm state of the el niño-southern oscillation cycle. *Meteorology and Atmospheric Physics*, *56*(1), 17–32.

Wang, W., & McPhaden, M. J. (2000). The surface-layer heat balance in the equatorial pacific ocean. part II: Interannual variability. *Journal of Physical Oceanography*, *30*(11), 2989–3008. doi: 10.1175/1520-0485(2001)031⟨2989:TSLHBI⟩2.0.CO;2

Watanabe, M., Dufresne, J. L., Kosaka, Y., Mauritsen, T., & Tatebe, H. (2020). Enhanced warming constrained by past trends in equatorial pacific sea surface temperature gradient. *Nat. Clim. Change*, *11*, 33-37.

Xie, S.-P., Kosaka, Y., & Okumura, Y. M. (2016). Distinct energy budgets for anthropogenic and natural changes during global warming hiatus. *Nature Geoscience*, *9*(1), 29–33. doi: 10.1038/ngeo2581

Yang, W., Vecchi, G. A., Fueglistaler, S., Horowitz, L. W., Luet, D. J., Muñoz, Á. G., ... Underwood, S. (2019). Climate impacts from large volcanic eruptions in a high-resolution climate model: The importance of forcing structure. *Geophysical Research Letters*, *46*(13), 7690–7699.

Yulaeva, E., & Wallace, J. (1994). The signature of ENSO in global temperature and precipitation fields derived from the microwave sounding unit. *Journal of Climate*.

Appendix A Supplemental Figures

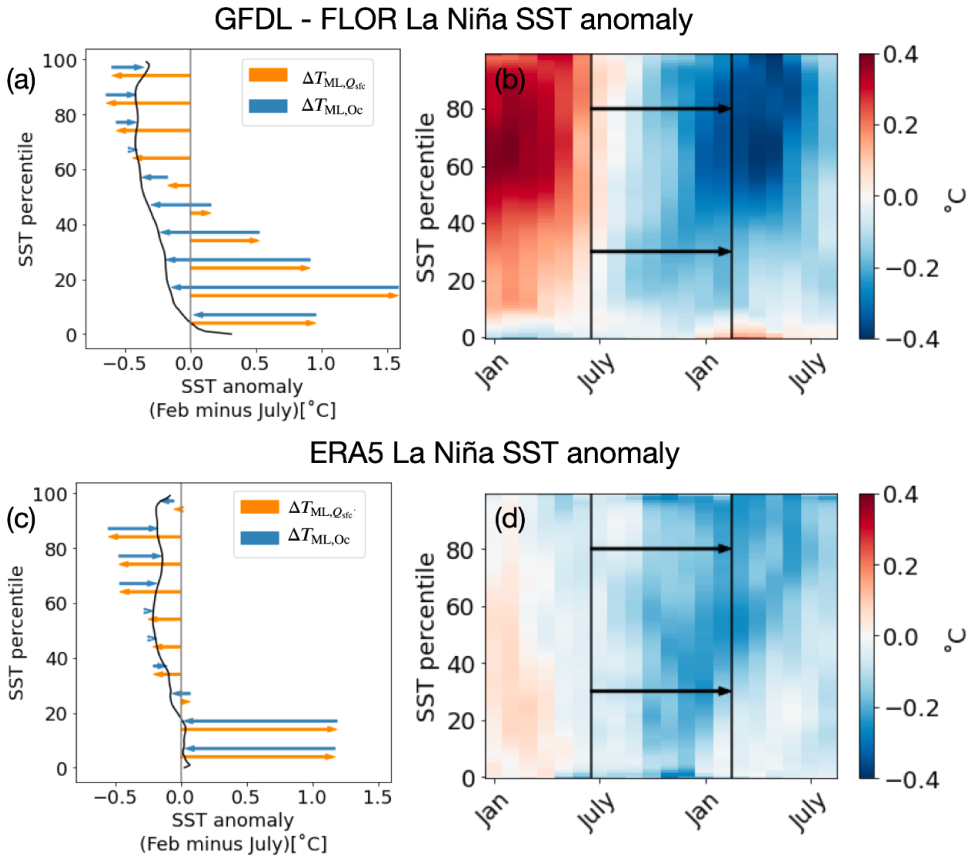

Figure A1. Contributions to ocean mixed-layer temperature decrease during La Niña. (a, c) ΔT_{ML} ($\approx$ ΔSST) at each percentile bin in the global tropics (30S:30N). $\Delta T_{\mathrm{ML},Q_{\mathrm{sfc}}}$ is represented by orange arrows and $\Delta T_{\mathrm{ML,Oc}}$ by blue arrows (calculated as a residual), both averaged over deciles (0-9th percentile, 10-19th percentile, etc.). (b, d) T_{ML} anomaly during a La Niña event, composited on the calendar year. Black lines are the limits for the integral represented in (a, c).

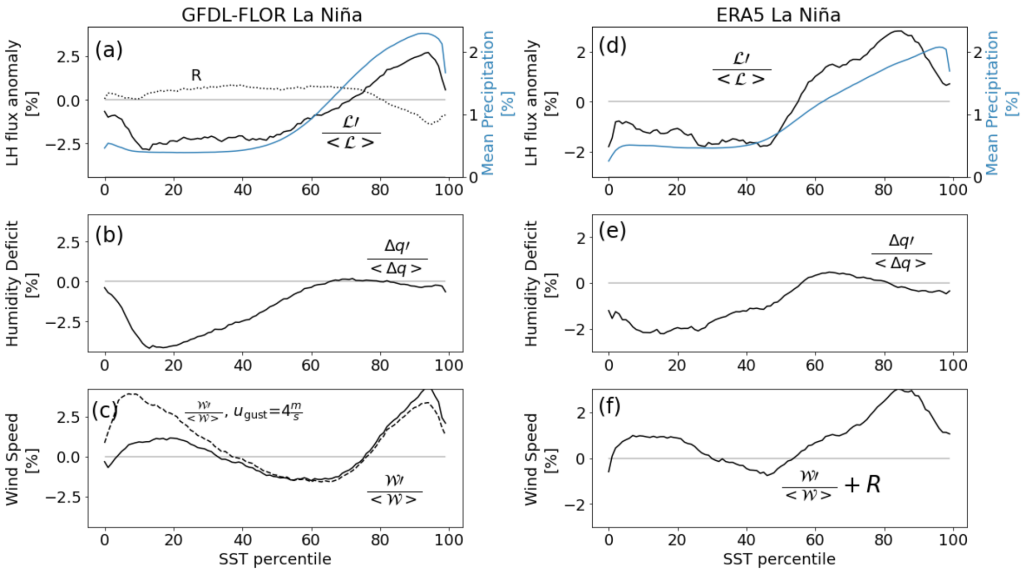

Figure A2. Latent heat flux anomaly during La Niña as a fraction of its climatological value Top (a, d): $\mathcal{L}$ anomaly and mean distribution of precipitation. Middle (b, e): humidity deficit Δq anomaly. Bottom (c, f): anomaly in the surface wind speed W. Solid lines in (b, c) approximate the solid black line in (a) with the residual R shown as the dotted line in panel (a) (Equation 3). (c) also shows an estimate of W if the gust speed is held constant at 4ms^{-1}. The wind speed anomaly shown in (f) is estimated as the residual of (d, e). All variables are sorted from coldest to warmest SST.

Figure 1.

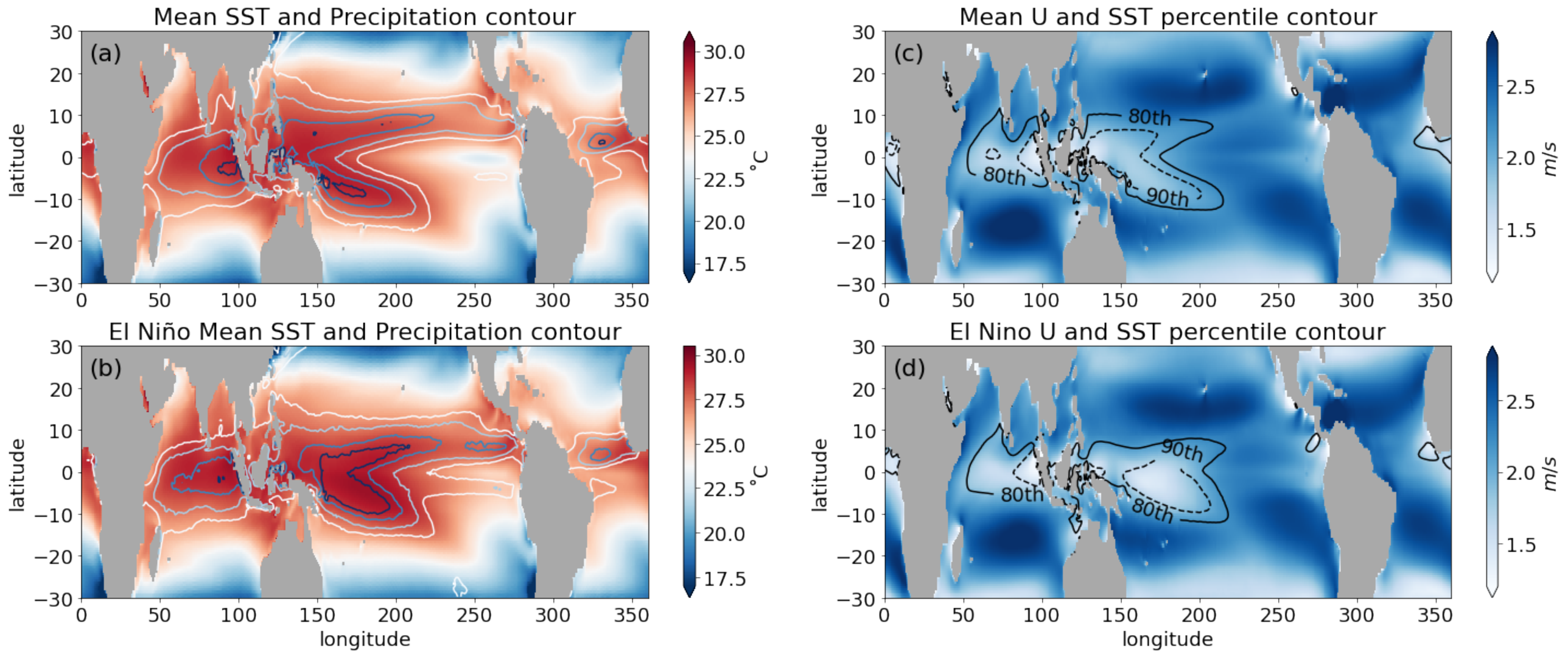
Mean SST and Precipitation contour
(a)
El Niño Mean SST and Precipitation contour
(b)
Mean U and SST percentile contour
(c)
80th
80th
90th
El Nino U and SST percentile contour
(d)
90th
80th
80th
latitude
longitude
°C
m/s
30.0
27.5
25.0
22.5
20.0
17.5
2.5
2.0
1.5
30
20
10
0
−10
−20
−30
0
50
100
150
200
250
300
350

Figure 2.

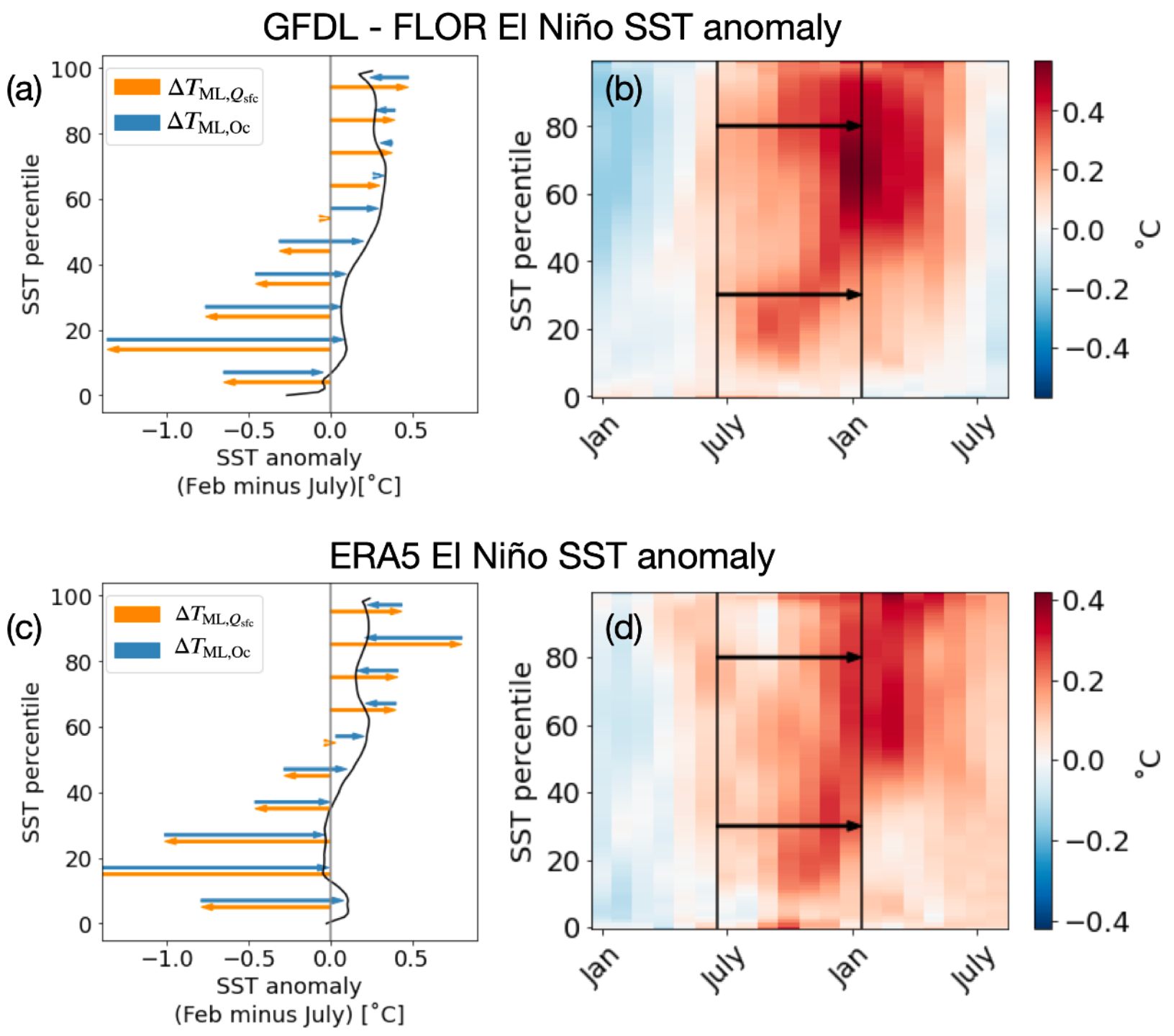
GFDL - FLOR El Niño SST anomaly
(a)
$\Delta T_{\mathrm{ML},Q_{\mathrm{sfc}}}$
$\Delta T_{\mathrm{ML,Oc}}$
SST percentile
SST anomaly
(Feb minus July)[˚C]
(b)
SST percentile
Jan
July
Jan
July
°C
ERA5 El Niño SST anomaly
(c)
$\Delta T_{\mathrm{ML},Q_{\mathrm{sfc}}}$
$\Delta T_{\mathrm{ML,Oc}}$
SST percentile
SST anomaly
(Feb minus July) [˚C]
(d)
SST percentile
Jan
July
Jan
July
°C

Figure 3.

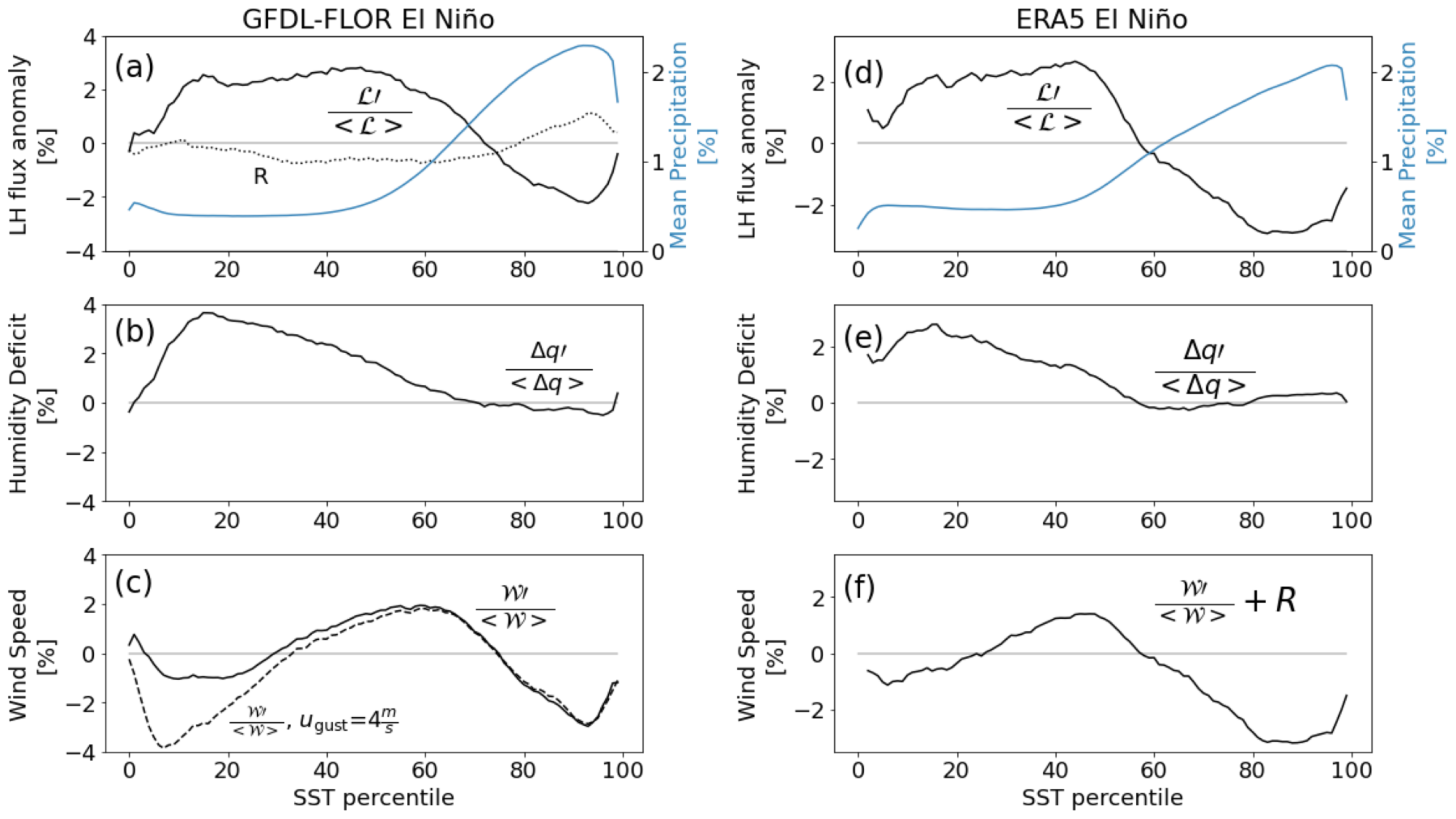
GFDL-FLOR El Niño
ERA5 El Niño
(a)
(b)
(c)
(d)
(e)
(f)
LH flux anomaly [%]
Humidity Deficit [%]
Wind Speed [%]
Mean Precipitation [%]
$\frac{\mathcal{L}\prime}{<\mathcal{L}>}$
R
$\frac{\Delta q\prime}{<\Delta q>}$
$\frac{w\prime}{<w>}$
$\frac{w\prime}{<w>}$, $u_{gust}=4\frac{m}{s}$
$\frac{w\prime}{<w>} + R$
SST percentile

Figure A1.

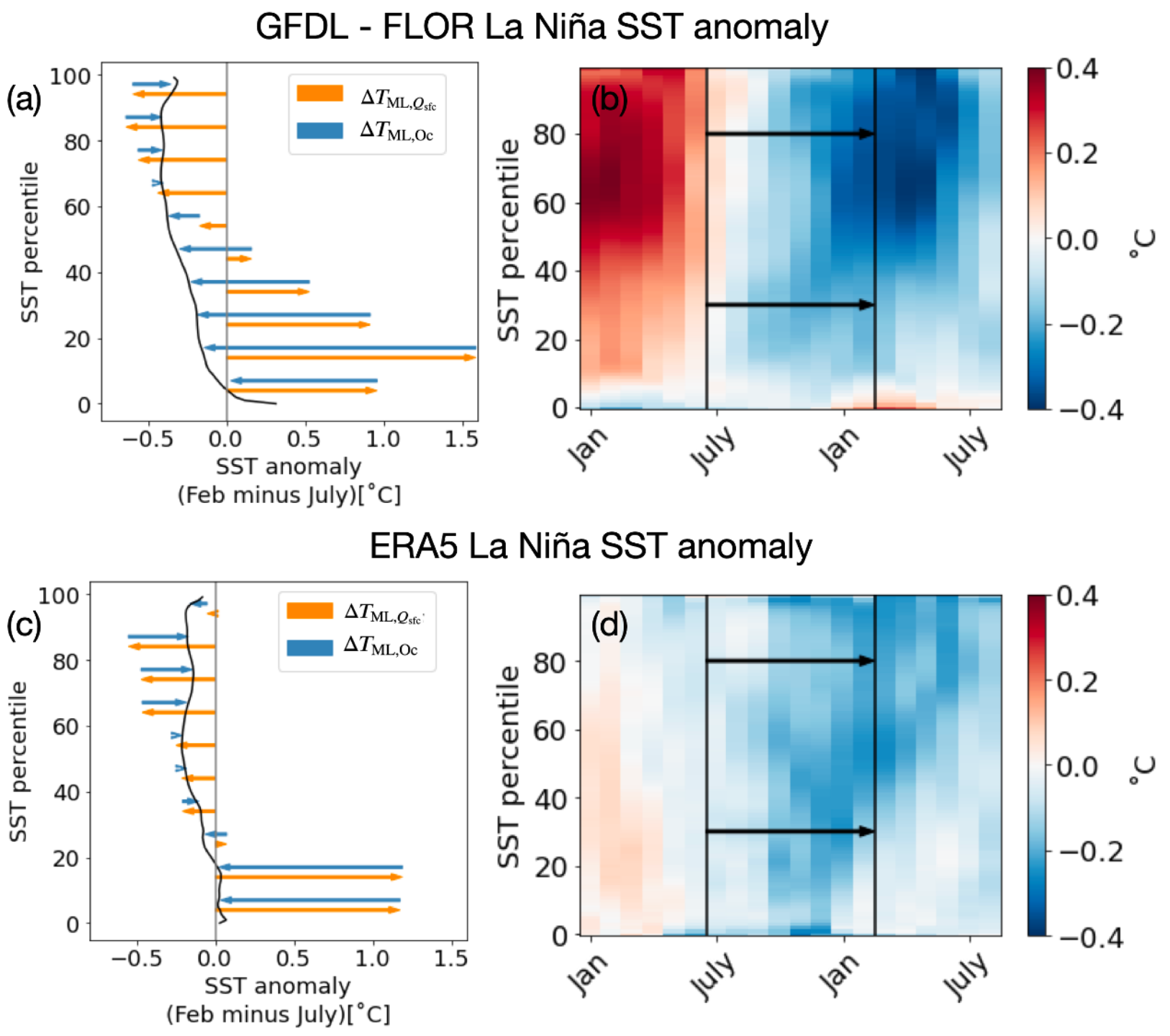
GFDL - FLOR La Niña SST anomaly
(a)
(b)
ERA5 La Niña SST anomaly
(c)
(d)
SST percentile
SST anomaly
(Feb minus July)[˚C]
Jan
July
°C

Figure A2.

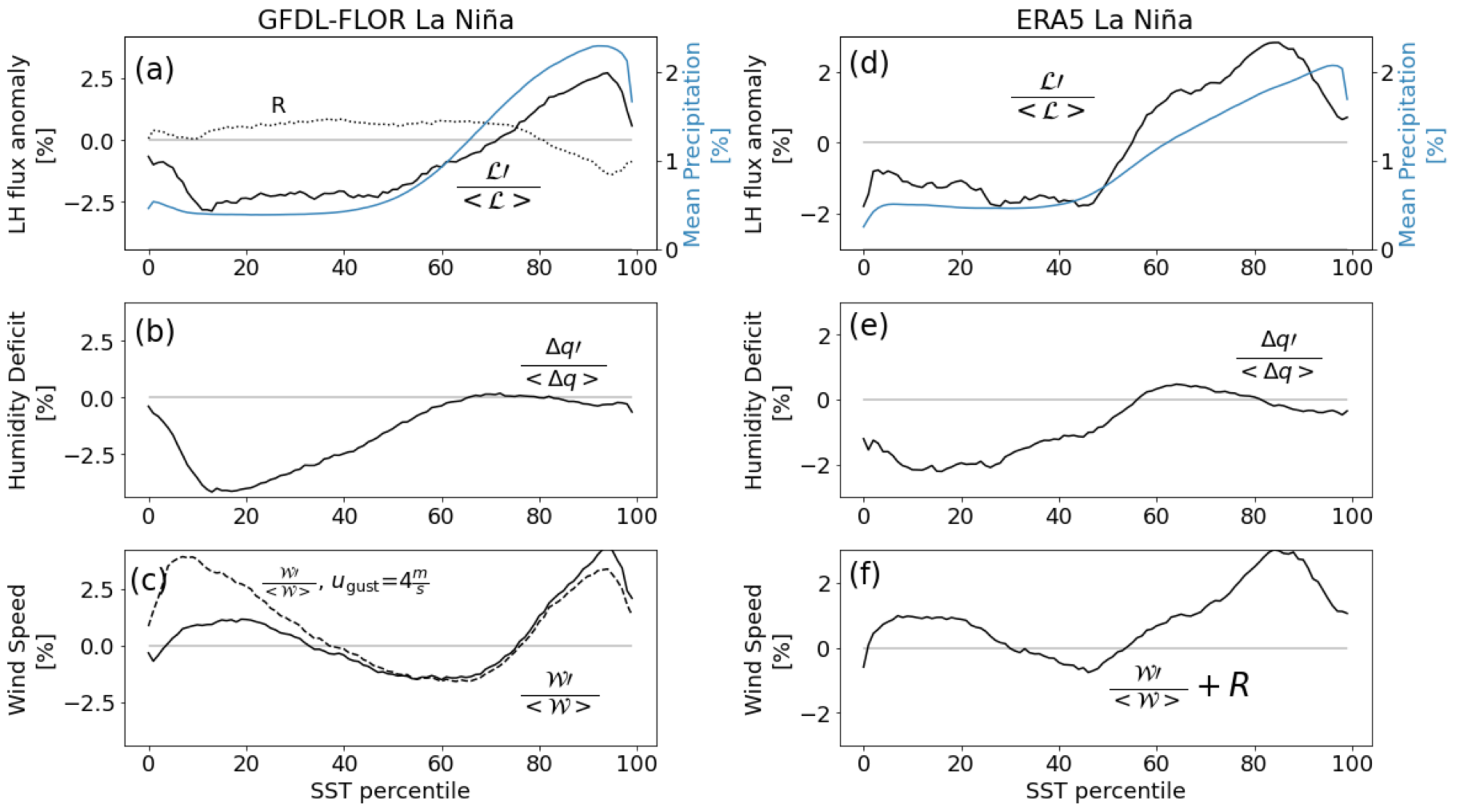
GFDL-FLOR La Niña
ERA5 La Niña
(a)
(b)
(c)
(d)
(e)
(f)
R
$\frac{\mathcal{L}\prime}{<\mathcal{L}>}$
$\frac{\Delta q\prime}{<\Delta q>}$
$\frac{w\prime}{<w>}$, $u_{gust}=4\frac{m}{s}$
$\frac{w\prime}{<w>}$
$\frac{w\prime}{<w>} + R$
LH flux anomaly [%]
Humidity Deficit [%]
Wind Speed [%]
Mean Precipitation [%]
SST percentile